ACS Catalysis

RESEARCH ARTICLE

pubs.acs.org/acscatalysis

Effects of Mo Replacement on the Structure and Visible-Light-Induced Photocatalytic Performances of Bi_2WO_6 Photocatalyst

Liwu Zhang, Yi Man, and Yongfa Zhu*

Department of Chemistry, Tsinghua University, Beijing 100084, P.R. China

Supporting Information

ABSTRACT: Phase-pure $Bi_2Mo_xW_{1-x}O_6$ ($0 \le x \le 1$) photocatalysts were synthesized via a hydrothermal method. The as-prepared $Bi_2Mo_xW_{1-x}O_6$ photocatalysts had an Aurivillius crystal structure and showed special anisotropic growth. The optical absorption spectra of $Bi_2Mo_xW_{1-x}O_6$ were red-shifted monotonically as the value of x increased. On the basis of theoretical calculations, the introduction of Mo atom into Bi_2WO_6 could reduce the conduction band level of Bi_2WO_6, so the band gap energy was reduced. The curvature of the conduction band became smaller with an increase in the Mo content due to the different electronegativities of Mo 4d and W 5d. The photocatalytic activities determined by rhodamine B degradation under visible light irradiation ($\lambda > 420$ nm) of $Bi_2Mo_xW_{1-x}O_6$ photocatalysts were significantly improved as compared with Bi_2MoO_6. The higher efficiency of Bi_2WO_6 was attributed to more effective photoelectron transfer in the conduction band with larger curvature. The photocatalytic activities under visible light irradiation ($\lambda > 450$ nm) of $Bi_2Mo_xW_{1-x}O_6$ photocatalysts were much higher than that of Bi_2WO_6. The mechanism was discussed on the basis of the cystal structure, morphology, and electronic stucture. This work provides a strategy for developing active photocatalysts with more utilization of visible light.

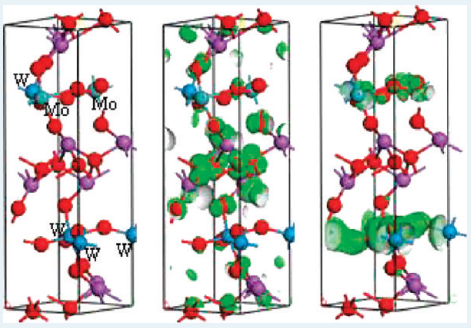

KEYWORDS: photocatalysis, Bi_2WO_6, Bi_2MoO_6, substitution, visible light

INTRODUCTION

Heterogeneous photocatalysts offer great potential for environmental remediation and for converting photon energy into chemical energy.[1−3] Typical examples are TiO_2-based photocatalytic decomposition of organic contaminants and water splitting.[1,2] Unfortunately, the band gap of TiO_2 is larger than 3.0 eV, which means it can show activity only under UV irradiation, so a great deal of effort has been devoted to developing visible-active TiO_2 photocatalysts.[4−7] Anions doping with N, C, and S or transition metal cation doping is commonly used to function TiO_2 as a visible light photocatalyst.[4−7] However, these doped TiO_2's show little absorption of the visible light; moreover, the photocatalytic activities are still very low due to complicated factors. Therefore, the development of efficient visible-light-active photocatalysts has been an urgent issue from the viewpoint of using solar energy.

The pioneering works done by Kudo et al. found that Bi_2WO_6 exhibited photocatalytic activities for O_2 evolution, and Zou revealed that Bi_2WO_6 could degrade the organic compound under visible light irradiation.[8,9] We have reported nanostructured Bi_2WO_6 photocatalysts could be synthesized via a hydrothermal method[10,11] and an amorphous complex precursor method,[12] and the photocatalysis experiment indicated that Bi_2WO_6 could perform as an excellent visible light photocatalyst for dye degradation; however, its efficiency of visible light utilization was still limited due to its absorption edge of 460 nm. Recently, Bi_2MoO_6 has been used as a visible light photocatalyst, and its absorption edge can be extended to 520 nm.[13−15] Bi_2MoO_6 possesses a much smaller band gap than that of Bi_2WO_6 and is a more ideal photocatalyst from the viewpoint of using visible light. Unfortunately, its photocatalytic activity is much lower than that of Bi_2WO_6.

Recent studies have shown that substitution of the M site ($A_xM_yO_z$) with other metal ions could considerably improve the catalytic activity.[16−18] The substitution of M sites might induce a slight modification of crystal structure due to the different ion radii, resulting in dramatic influence on the mobility of the charge carrier and change the photocatalytic and photophysical properties.[19] Moreover, the optical response could also be changed due to the substitution, which could change the d electronic configuration. Therefore, from the viewpoint of developing a highly efficient Bi_2WO_6 photocatalyst with a wider optical response in the visible spectral range, the substitution of W sites in Bi_2WO_6 with Mo is studied in the present work. W substitution for Mo in Bi_2MoO_6, and $Bi_2Mo_{1-x}W_xO_6$ with single phases have been prepared by solid state reaction and mechanochemical activation to improve the ferroelectric property of Bi_2MoO_6.[20] $Bi_2Mo_xW_{1-x}O_6$ solid solutions with adjustable band gaps have been prepared by Yu's group via hydrothermal treatments, and the visible-light-induced

Received: March 23, 2011
Revised: April 29, 2011
Published: June 01, 2011

photocatalytic activity of Bi_2WO_6 was found to be improved with a certain content of Mo substitution.[21] However, the mechanism of the effects of Mo replacement on the local structures and photocatalytic activities of Bi_2WO_6 photocatalysts is still not very clear. Theoretical studies using density functional theory (DFT) calculations for the purpose of probing the correlation between band structure and photocatalytic activity in substituted photocatalysts are still reported poorly. Herein, $Bi_2Mo_xW_{1-x}O_6$ ($0 \le x \le 1$) photocatalysts were synthesized, and the mechanism of the effects of Mo replacement on the photocatalytic activities of Bi_2WO_6 photocatalysts were systematically studied on the basis of the crystal structure, electronic structure, and morphology of Bi_2WO_6 photocatalysts revealed by X-ray diffraction; density functional theory (DFT) calculations; transmission electron microscopy, UV−visible diffuse reflection spectra, Raman spectra, etc.

EXPERIMENTAL SECTION

Preparation. $Bi_2Mo_xW_{1-x}O_6$ nanosheets with x = 0, 0.05, 0.25, 0.5, 0.75, 0.95, 1 were synthesized via a simple hydrothermal method. $Bi(NO_3)_3 \cdot 5H_2O$, $(NH_4)_6Mo_7O_{24} \cdot 6H_2O$, and H_2WO_4 were chosen as starting metal sources in stoichiometric proportion to form $Bi_2Mo_xW_{1-x}O_6$. All chemicals used were analytical grade reagents without further purification. The starting chemicals were mixed together, and 10 mL of deionized water was added. The pH value of the precursor solution was adjusted to 7 with 1 mol/L KOH. The solution and precipitate were added into a 40 mL Teflon-lined autoclave and filled with deionized water up to 80% of the total volume. Then the autoclave was sealed into a stainless steel tank and kept at 180 °C for 24 h. Then the autoclave was cooled to room temperature naturally. After cooling, the yellow precipitate was washed with deionized water and dried at 80 °C in an oven.

Characterization. Crystallinity of the as-prepared samples were characterized by powder X-ray diffraction (XRD) on a Bruker D8 Advance X-ray diffractometer with Cu Kα radiation and a 2θ scan rate of 2°/min. The morphology and particle sizes of samples were determined by a JEOL JEM-1200EX transmission electron microscope (TEM) at 120 kV. UV−vis diffuse reflectance spectra (DRS) were recorded in the range 200−700 nm using $BaSO_4$ as the reference sample in a Hitachi U-3010 spectroscope. Raman spectra were recorded on a RM 2000 microscopic confocal Raman spectrometer (Renishaw Company) with an excitation of 514 nm laser light at 0.5 mW and were accumulated three times for 30 s each. The spectra were recorded with a charge-coupled device camera. The Brunauer−Emmet−Teller surface area was determined by nitrogen absorption−desorption isotherm measurements at 77 K on a nitrogen absorption apparatus (Micrometrics ASAP 2010).

Photoreactor. The visible light source was a 500 W xenon lamp (Institute of Electric Light Source, Beijing) that was positioned beside a cylindrical reaction vessel and cooled to maintain the ambient temperature. Cutoff filter (λ > 420 nm or λ > 450 nm, bought from Nantong Xiangyang Optical Element Co., Ltd.) was placed upside the vessel. The average light intensity was 35 mW/cm^2 at the surface of the solution. The photocatalytic experiments were performed at a temperature of 25 °C.

Procedure and Analyses. Aqueous suspensions of RhB (100 mL, 1×10^{-5} M) and 100 mg of $Bi_2Mo_xW_{1-x}O_6$ powder photocatalysts were placed in the vessel. Prior to irradiation, the suspensions were dispersed in an ultrasonic bath for 10 min and then magnetically stirred for 10 min in the dark to ensure the establishment of adsorption/desorption equilibrium. At given time intervals, 4 mL of liquid was sampled and centrifuged to remove the particles. The filtrates were then analyzed by the Hitachi U-3010 UV−vis spectrophotometer.

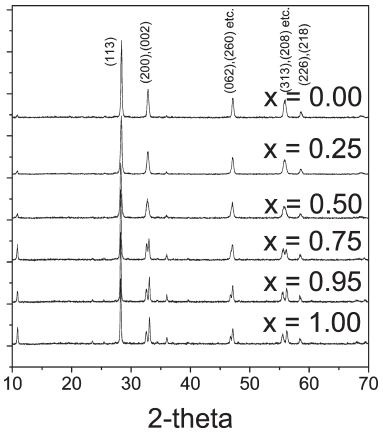

Figure 1. X-ray diffraction patterns of $Bi_2Mo_xW_{1-x}O_6$.

RESULTS AND DISCUSSION

Effects of Mo Replacement on Crystal Structure of Bi_2WO_6 Photocatalysts. XRD patterns of $Bi_2Mo_xW_{1-x}O_6$ samples are shown in Figure 1. It can be observed that $Bi_2Mo_xW_{1-x}O_6$ samples with single Aurivillius phase can be synthesized via a hydrothermal method, which was also reported by Yu's group,[21] in which the Mo powder and W powder dissolved in H_2O_2 were used as the metal source. In the current work, $(NH_4)_6Mo_7O_{24} \cdot 6H_2O$ and H_2WO_4 were directly utilized without further treatment to synthesize the $Bi_2Mo_xW_{1-x}O_6$ with a single Aurivillius phase.

The diffraction peaks of Bi_2WO_6 and Bi_2MoO_6 can be exactly indexed as JCPDS 79-2381 and 21-0102, respectively. The similarity of the diffractograms suggests that these compounds are isostructural with Aurivillius Bi_2WO_6, with slight shifts in the 2θ values being observed for several diffraction peaks (peaks at 2θ = 10.8°, 28.4°, and 47.0°). The standard intensity of the (113) peak was about 5 times that of the (200) or (010) peak, whereas the I(113)/I(200) of the samples was smaller than 2, implying the as-prepared Bi_2WO_6 nanoparticles had special anisotropic growth,[10] in accordance with the nanoplate morphologies observed by TEM.

Meanwhile, it was observed that the $Bi_2Mo_xW_{1-x}O_6$ samples also had special anisotropic growth. The enlarged parts of Figure 1 with XRD patterns from 27° to 35° are shown in Figure 2a. It was noteworthy that the (113) diffraction peaks of $Bi_2Mo_xW_{1-x}O_6$ samples shifted to a lower angle with the increase in the Mo content in the compounds. Mo has a slightly smaller atomic radius than W (134.2 vs 137 pm); however, the effective electronegativity of 4d transition metal ions is higher than their 5d counterparts, and as a consequence, they should be expected to form more covalent bonds with oxygen, which would slightly modify the crystal structure and could be the reason for the lower angle shift of the (113) diffraction peaks.[22] It is also observed in Figure 2a that the (113) diffraction peak is sharpened as the Mo content increases, indicating the crystallite size is larger when Mo atoms are incorporated, in accordance with the TEM images.

The evolution of the lattice parameters with the composition is shown in Figure 2b, c, d. The cell constants of a, b, c values were calculated on the basis of the orthorhombic symmetry reported

dx.doi.org/10.1021/cs200155z |ACS Catal. 2011, 1, 841–848

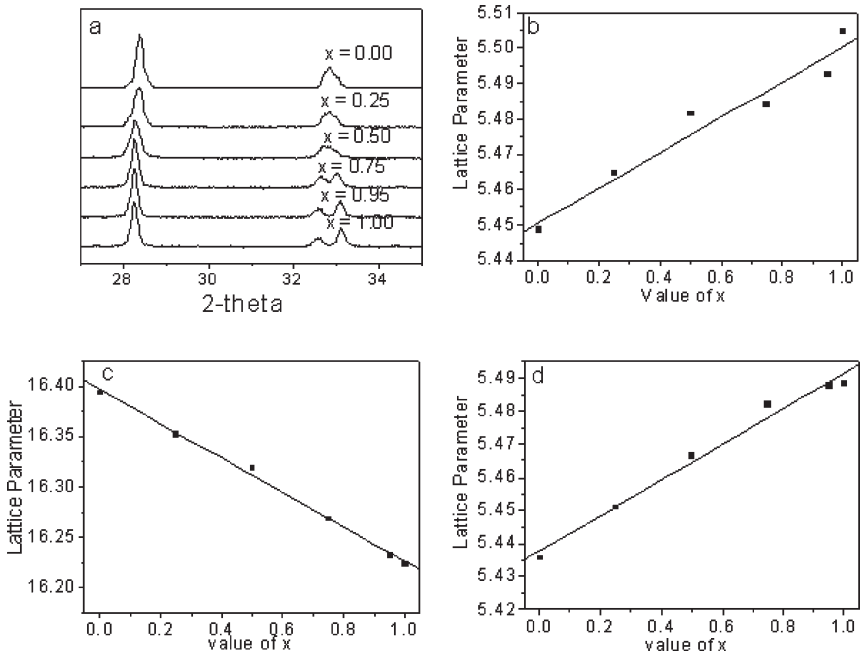

Figure 2. (a) The enlarged XRD patterns part of $Bi_2Mo_xW_{1-x}O_6$ ranging from $2\theta = 27$ to 35°; (b–d) The lattice parameter of *a*, *b*, *c*, respectively, of $Bi_2Mo_xW_{1-x}O_6$.

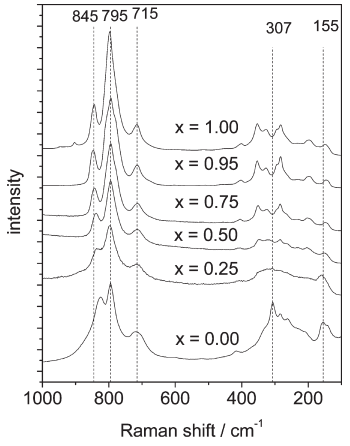

Figure 3. Raman spectra for prepared $Bi_2Mo_xW_{1-x}O_6$.

in the JCPDS card file of Bi_2WO_6. With the increased content of Mo, the value of *a*, *c* increase regularly, while the value of *b* decreases. Interestingly, the calculated cell volume increases with increasing Mo content, although Mo possesses a slightly smaller atomic radius, which is in accordance with the cell volume data from ICSD database for Bi_2WO_6 and Bi_2MoO_6 (487.6 vs 489.2). The shifted XRD peaks and the changes of the lattice parameters indicate that the direct substitution of Mo^{6+} for the W site in Bi_2WO_6 is possible, and the ternary compounds were synthesized as single $Bi_2Mo_xW_{1-x}O_6$ phases corresponding to a continuous series of solid solutions between Bi_2WO_6 and Bi_2MoO_6.

Raman spectra of $Bi_2Mo_xW_{1-x}O_6$ samples are shown in Figure 3. In general, all Raman bands for Bi_2WO_6 above 400 cm^{-1} were assigned to W–O stretching modes and were assumed to reflect directly W–O bond lengths in tungstate species.[23] The peaks in the range 600–1000 cm^{-1} were assigned to the stretches of the W–O bands. In more detail, the bands at 790 and 820 cm^{-1} were associated with antisymmetric and symmetric A_g modes of the WO_6 octahedra that involve motions of the apical oxygen atoms that are perpendicular to the layers.[24] Raman bands observed in the range 600–1000 cm^{-1} for Bi_2MoO_6 were assigned to Mo–O stretches, and those below 400 cm^{-1} were assigned to bending, wagging, and external modes by directly correlating Mo–O bond lengths.[25] A strong band at 795 cm^{-1} along with two shoulder bands at 845 and 714 cm^{-1} of Bi_2MoO_6 were observed, corresponding to Mo–O stretching modes of the distorted MoO_6 octahedra. It is notable that with the increasing Mo content, the band at 820 cm^{-1} is shifted to higher wavenumbers, which could be attributed to the different metal–oxygen bond lengths within WO_6 and MoO_6 octahedra related to the apical oxygen atoms. However, the mode at 715 cm^{-1} exhibits no evident shift and broadening, which is due to the asymmetric stretching vibration (E_u mode) of the WO_6 octahedra involving the motion of the equatorial oxygen atoms within layers, further confirming that the variation of WO_6 structure exists in only the apical oxygen atoms, not equatorial oxygen atoms. The relationship between Raman stretching frequency and bond length was found to follow a simple exponential form,

$$R_{W-O} = 0.48239 \ln(32895/\nu)$$

where ν is the Raman stretching frequency in wavenumbers and *R* is the metal–oxygen bond length in angstroms. It can be concluded that the lower frequencies of the Raman stretching band correspond to the longer bond lengths. With the increasing Mo content, the band at 820 cm^{-1} is shifted to higher wavenumbers, indicating the apical W–O bond length is decreased.

Morphologies of $Bi_2Mo_xW_{1-x}O_6$ Samples and Effects of Mo Replacement on Surface Area and Pore Size Distribution. Morphologies of $Bi_2Mo_xW_{1-x}O_6$ samples were investigated by TEM; the result is shown in Figure 4. Figure 4a and f shows the morphologies of Bi_2MoO_6 and Bi_2WO_6 samples, respectively. It is observed that the Bi_2WO_6 particles have a sheetlike morphology, whereas the Bi_2MoO_6 particles have a much

dx.doi.org/10.1021/cs200155z |ACS Catal. 2011, 1, 841–848

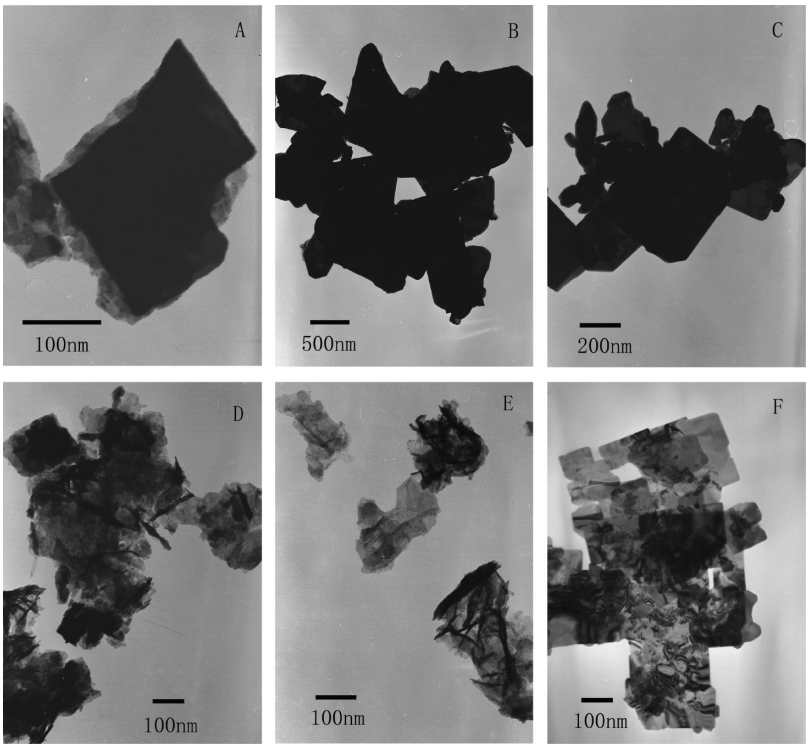

Figure 4. TEM micrographs of $Bi_2Mo_xW_{1-x}O_6$ samples; x = (A) 1, (B) 0.95, (C) 0.75, (D) 0.25, (E) 0.05, and (F) 0.

thicker platelike morphology. The sheetlike and platelike morphologies indicate a preferential growth of the crystal, in accordance with the XRD results. Figure 4b−e shows the morphologies of $Bi_2Mo_xW_{1-x}O_6$ from $x = 0.95$ to $x = 0.05$. With the decrease in x, the particles became smaller and thinner. The sample of $Bi_2Mo_{0.05}W_{0.95}O_6$ has an average particle size of ∼200 nm, but the particle size of $Bi_2Mo_{0.95}W_{0.05}O_6$ is ∼700 nm. Moreover, the thickness of the latter particles is also much greater, so it could be concluded that the substitution of the Mo atom for the W atom may significantly influence the crystal growth and the tungstate prefers to form nanosheet morphology when the amount of Mo is lower.

Figure 5 shows the nitrogen adsorption−desorption isotherm for $Bi_2Mo_xW_{1-x}O_6$ samples. The nitrogen adsorption isotherms and pore size distributions of $Bi_2Mo_xW_{1-x}O_6$ with x = 1, 0.25, 0.05, and 0 are shown in Figure 5a−d, respectively. The adsorption isotherms for all these samples can be assigned as type II, which is characteristic of nonporous or macroporous solids in BDDT classification.[26] In addition, the hysteresis loop resembled H3 in IUPAC classification, which did not exhibit any limiting adsorption at high relative pressure. These results indicate that the adsorbents do not possess well-defined mesoporous structures. A pore-size-distribution curve was calculated from the desorption branch of nitrogen isotherm by the BJH method. The pore size ranges of Bi_2MoO_6, $Bi_2Mo_{0.25}W_{0.75}O_6$, $Bi_2Mo_{0.05}W_{0.95}O_6$, and Bi_2WO_6 were 0−160, 0−90, 0−160, and 0−140 nm, respectively, and the main pore sizes were 80, 30, 25, and 20 nm, respectively. With the increased Mo content in $Bi_2Mo_xW_{1-x}O_6$ samples, the pore size is also increased. The surface area for Bi_2MoO_6 was 16.39 m^2/g, whereas the surface area for Bi_2WO_6 was 42.89 m^2/g. From $x = 0.05$ to $x = 0.95$, the surface areas of $Bi_2Mo_xW_{1-x}O_6$ decreased from 33.6 to 20.24 m^2/g, in accordance with the TEM results, which showed the samples possess a larger particle size with more Mo atoms in the sample.

Effects of Mo Replacement on the Optical Properties of Bi_2WO_6. Figure 6 shows the DRS spectra of the $Bi_2Mo_xW_{1-x}O_6$ samples. It is found that the DRS spectra of $Bi_2Mo_xW_{1-x}O_6$ samples possessed steep edges in the profile, indicating that the visible light absorption was not caused by the transition from the impurity level but was due to the band gap transition.[27] From the onsets of the absorption, the band gaps of Bi_2MoO_6 and Bi_2WO_6 were estimated to be 2.36 and 2.7 eV, respectively. The absorption edges of $Bi_2Mo_xW_{1-x}O_6$ were located in a position between those of Bi_2MoO_6 and Bi_2WO_6, and the absorption spectra were red-shifted as the value of x increased. The band gap energies estimated from the $(\text{absorbance})^{0.5}(h\nu)^{0.5}$ versus photon energy plots were 2.56, 2.46, 2.44, 2.43, and 2.42 eV, respectively, for $Bi_2Mo_xW_{1-x}O_6$ with x = 0.05, 0.25, 0.5, 0.75, and 0.95, respectively. The difference of band gaps in the photocatalysts might result from the conduction band. Mo^{6+} substituting can decrease the conduction band level of Bi_2WO_6. It is noteworthy that the onset of the diffuse reflection spectra with Mo substitution is not linearly shifted. The overall band gap of a given $Bi_2Mo_xW_{1-x}O_6$ compound can be thought to depend mainly upon two factors: (i) the degree of Mo 4d and W 5d orbitals being involved in the conduction band of $Bi_2Mo_xW_{1-x}O_6$ and (ii) the degree of delocalization of excitation energy due to the distortion of the crystal structure arising from Mo substitution. It may thus be said that change in the band gap energy is not necessarily proportional to that in the amount of Mo substitution. A similar result was also reported in $Sr_2Nb_{2-x}Ta_xO_7$[18] and $Ca_2Nb_{2-x}Ta_xO_7$ solid solution.[28]

Effects of Mo Replacement on Electronic Structure of Bi_2WO_6. The quantum-mechanical calculations performed here are based on density functional theory.[29] Exchange-correlation effects were taken into account by using the generalized gradient approximation.[30] The total energy code CASTEP was used,[31,32]

dx.doi.org/10.1021/cs200155z |ACS Catal. 2011, 1, 841–848

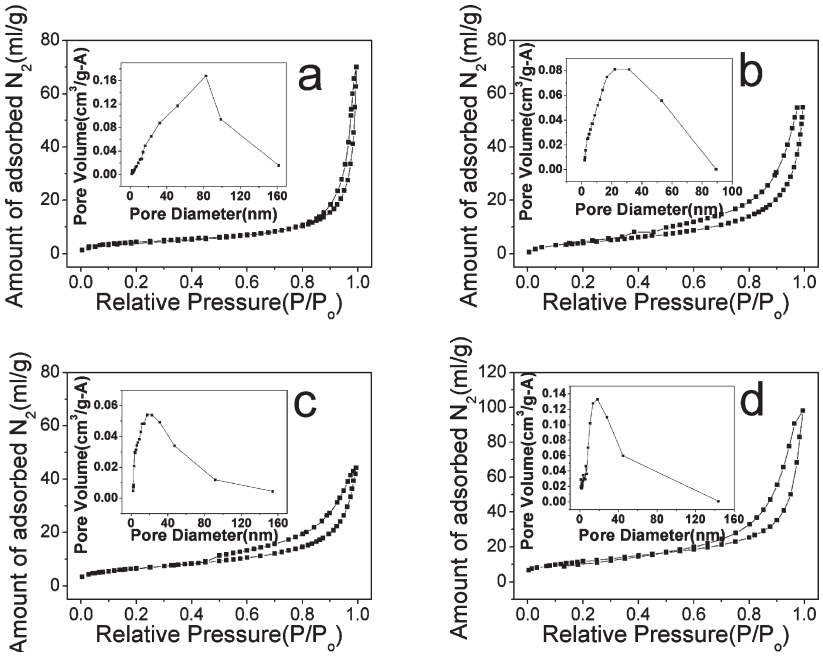

Figure 5. Nitrogen adsorption−desorption isotherms and pore size distribution curves for series prepared $Bi_2Mo_xW_{1-x}O_6$. x = (a) 1, (b) 0.25, (c) 0.05, and (d) 0;.

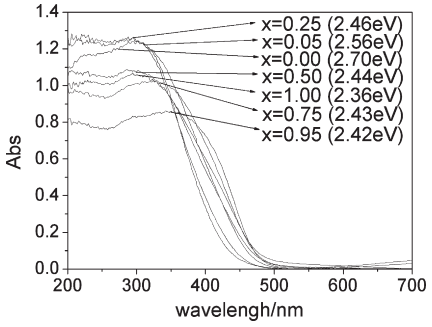

Figure 6. Diffuse reflectance spectra of a series of prepared $Bi_2Mo_xW_{1-x}O_6$ crystallines.

which utilizes pseudopotentials to describe electron−ion interactions and represents electronic wave functions using a plane-wave basis set. The kinetic energy cutoff was set at 380 eV.

Herein, the electronic structures of Bi_2WO_6 and $Bi_2Mo_{0.33}W_{0.67}O_6$ were investigated. The model of $Bi_2Mo_{0.33}W_{0.67}O_6$ was built by replacing two W atoms with Mo in a primitive cell of Bi_2WO_6 (Figure 8a). The P(−1) crystal symmetry was preserved to give these models. The structure was optimized with a constraint of lattice parameters.

The calculated band dispersions and densities of states for $Bi_2Mo_{0.33}W_{0.67}O_6$ are shown in Figure 7. The top of the valence band corresponds to orbital 108, and the bottom of the conduction band corresponds to orbital 109. The contents of each band are shown in Figure 7a. For example, orbitals 77−108 were composed of O 2p + Bi 6s6p orbitals. The band gap lies between orbitals 108 and 109. The valence band was composed of O 2p + Bi 6s6p and Bi 6p + O 2p + W 5d + Mo 4d, whereas the conduction band was composed of W 5d and Mo 4d orbitals. The conduction band also contains small contributions from Bi 6p orbitals by the overlap with W 5d and Mo 4d orbitals. The band gap was reasonably estimated to be 0.53 eV, taken as the energy difference between the top of the O 2p + Bi 6s band and the bottom of the W 5d + Mo 4d + Bi 6p band. The PDOS (partial density of states) of Bi, W, Mo, and O atoms are shown in the Supporting Information (Figures 1S and 2S). Figure 7b shows the composition of the density of states for Bi_2WO_6 and $Bi_2Mo_{0.33}W_{0.67}O_6$.

Figure 8 indicates the evolution of the electronic structure with the increased Mo content in Bi_2WO_6. The valence bands of all compounds were similar, but the potential level of the conduction band of $Bi_2Mo_{0.33}W_{0.67}O_6$ and Bi_2MoO_6 was lower than that of Bi_2WO_6. Generally, the potential level of the conduction band was lowered as the amount of Mo increased. The XPS valence band spectra have been reported and discussed by Yu's group.[21] In their work, a similar value of the VB maximum was observed from the XPS valence band spectra; this could be attributed to the similar compostion of the VB maximum (O 2p + Bi 6s6p) based on the DFT calculation. The difference in the width of the VB could be attributed to the incorporation of Mo 4d at the lower part of VB. The substitution of Mo in Bi_2WO_6 would reduce the conduction band level of Bi_2WO_6 because the Mo 4d band was involved in the conduction band, so the band gap of $Bi_2Mo_xW_{1-x}O_6$ decreased as the value of x increased, which is in accordance with the results of diffuse reflection spectra. It is noteworthy that a larger curvature is observed in the conduction band of Bi_2WO_6 than that of $Bi_2Mo_{0.33}W_{0.67}O_6$ and Bi_2MoO_6. As a consequence, the widths of the conduction of $Bi_2Mo_{0.33}W_{0.67}O_6$ and Bi_2MoO_6 are 2.2 and 2.0 eV, respectively, which are narrower than that of Bi_2WO_6 (2.5 eV). Namely, the width of the conduction and curvature decreased as the amount of Mo increased. The mobility of the electronic carrier is proportional to the reciprocal effective mass of carrier, which is in proportion to the curvature.[33] This means that Bi_2WO_6 has a larger electron mobility than $Bi_2Mo_{0.33}W_{0.67}O_6$ and Bi_2MoO_6.

dx.doi.org/10.1021/cs200155z |ACS Catal. 2011, 1, 841–848

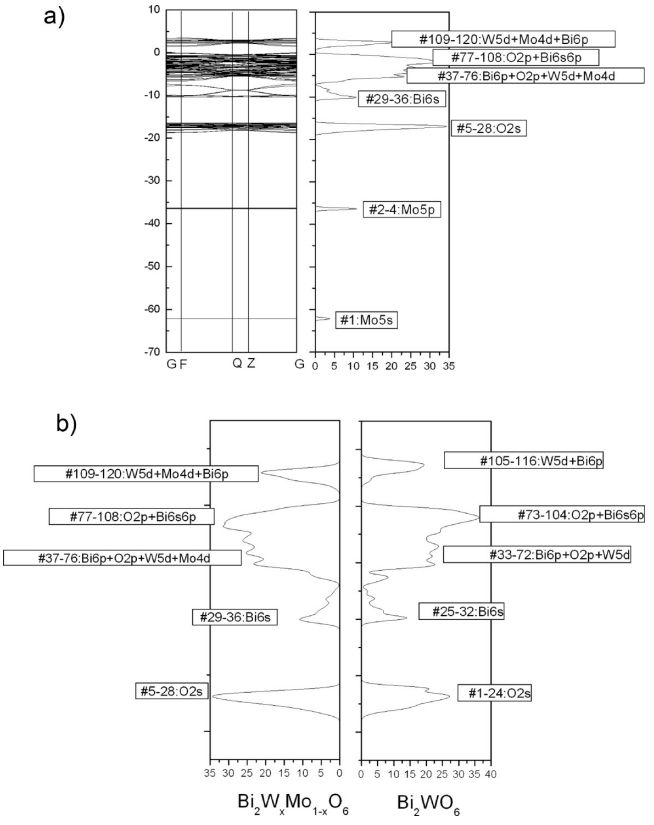

Figure 7. (a) Energy-band diagram and density of states for $Bi_2Mo_xW_{1-x}O_6$ with x = 0.333 calculated by a DFT method; (b) Comparison of density of states between Bi_2WO_6 and $Bi_2Mo_xW_{1-x}O_6$ with x = 0.333.

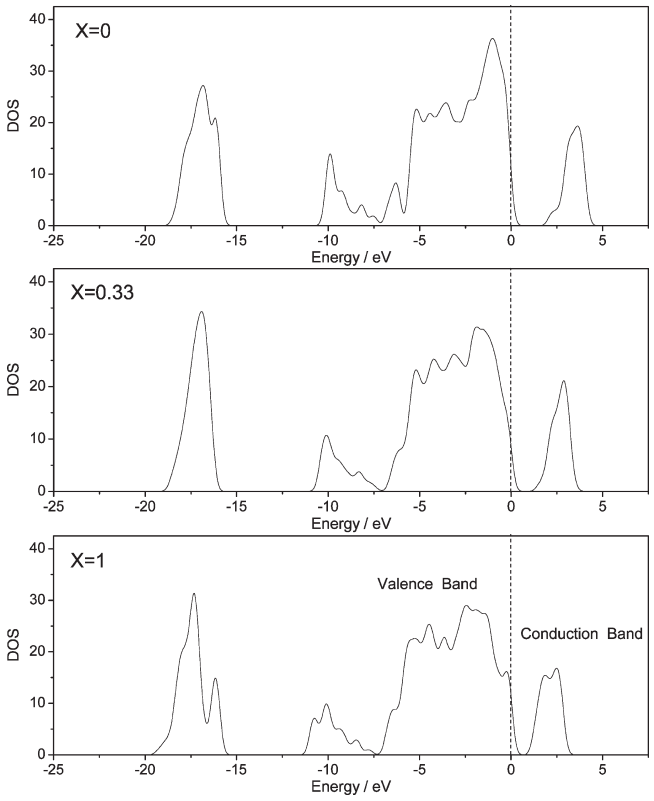

Figure 8. The evolution of electronic structure with the increased amount of Mo.

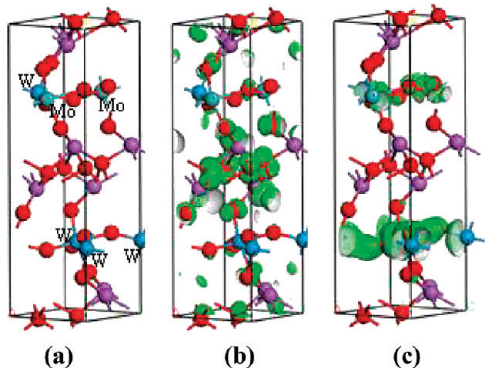

Figure 9. (a) The optimized model of Mo-doped Bi_2WO_6. (b) Electron density contour map for the top of the valence band (HOMO). (c) Electron density contour map for the bottom of the conduction band (LUMO). Purple, blue, and red balls represent Bi, W, and O atoms, respectively.

The optimized model of $Bi_2Mo_{0.33}W_{0.67}O_6$ and the electron density contour maps for the top of valence band (HOMO) and bottom of conduction band (LUMO) are shown in Figure 9. Orbital 108 was the top of the valence band. This orbital, shown in Figure 9b, was formed by the O 2p orbital with a small mixing of Bi 6s. The contour map of orbital 109, the bottom of the conduction band, is shown in Figure 9c; the electron density was localized to W 5d and Mo 4d orbitals only. The upper part of the conduction band consists of W 5d, Mo 4d, and O 2p orbitals, whereas the lower part was composed of W 5d and Mo 4d orbitals only. The contour map of the upper part is not shown.

Effects of Mo Replacement on Photocatalytic Activities of Bi_2WO_6. RhB photodegradation was used as a model reaction to evaluate the photoactivities of the as-prepared samples. The photodegradation of RhB under visible light (λ > 420 nm) is shown in Figure 10. The first-order linear relationship was revealed by the plots of $\ln(C/C_0)$ vs irradiation time (t). When x = 0.05 and 0.25, the photocatalytic activities of $Bi_2Mo_xW_{1-x}O_6$ were better than that of the Bi_2MoO_6 sample, but they were lower than that of the Bi_2WO_6 sample. From x = 0.5 to x = 0.95, the photocatalytic activities of $Bi_2Mo_xW_{1-x}O_6$ were lower than Bi_2MoO_6. The determined reaction rate constants (k) were 0.045, 0.014, 0.0218, 0.0053, 0.0021, 0.0025, and 0.00834 min^{-1} for x = 0, 0.05, 0.25, 0.5, 0.75, 0.95, 1, respectively.

Bi_2WO_6 and Bi_2MoO_6 were synthesized with identical preparation process, but the photocatalytic activity of Bi_2WO_6 was ~5 times higher as compared with Bi_2MoO_6. One reason could be the surface area. The surface area of Bi_2WO_6 was 3 times bigger than that of Bi_2MoO_6. A big surface area is greatly favored for the photocatalytic degradation of RhB. Another reason that must be considered is the different electronegativities of W and Mo ions. Band structure calculations performed on Mo-substituted Bi_2WO_6 found that the curvature of conduction band becomes smaller. The pentavalent ions W^{6+} and Mo^{6+} are often thought of as almost interchangeable, because they have nearly identical ionic radii and oftentimes very similar crystal chemistry. However, the effective electronegativity of 4d transition metal ions is higher than their 5d counterparts, and as a consequence,

dx.doi.org/10.1021/cs200155z |ACS Catal. 2011, 1, 841–848

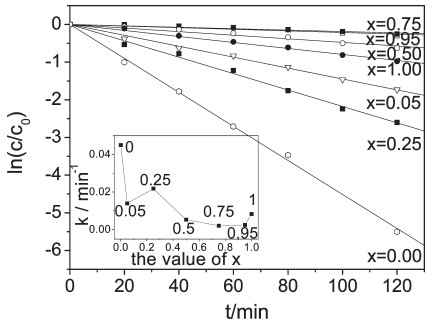

Figure 10. First-order plots for the photocatalytic degradation of RhB for prepared $Bi_2Mo_xW_{1-x}O_6$ under visible light irradiation $\lambda > 420$ nm. The inset is the plot of the apparent reaction rate constant (k).

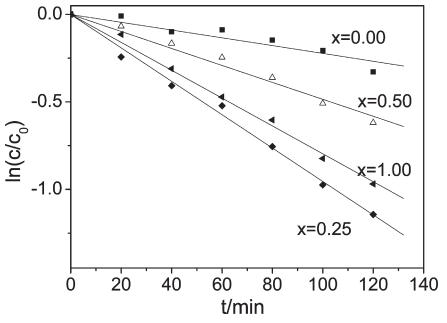

Figure 11. First-order plots for the photocatalytic degradation of RhB for prepared $Bi_2Mo_xW_{1-x}O_6$ under the irradiation of visible light $\lambda >$ 450 nm.

they should be expected to form more covalent bonds with oxygen, which results in the formation of a narrower conduction band with a smaller curvature and a possible delocalization of the charge carriers. More covalent bonds, resulting in a relatively narrow conduction band with a smaller curvature, were not effective for the movement of photogenerated electron−hole pairs.[34,35] Consequently, Bi_2WO_6 had a higher photocatalytic activity than Bi_2MoO_6.

As the structure of $Bi_2Mo_xW_{1-x}O_6$ changed from Bi_2WO_6 to Bi_2MoO_6 with x increasing, the photocatalytic activities of $Bi_2Mo_xW_{1-x}O_6$ decreased as the value of x increased. It is worth noting that at $x = 0.05$ and $x = 0.95$, the photocatalytic activities of $Bi_2Mo_{0.05}W_{0.95}O_6$ and $Bi_2Mo_{0.95}W_{0.05}O_6$ were lower than the samples with more Mo substitution: $Bi_2Mo_{0.25}W_{0.75}O_6$ and Bi_2MoO_6, respectively. Both of these samples possess a low level substitution. Low-level substitution of W(Mo) in $Bi_2W(Mo)O_6$ with Mo(W) would produce more defects, which could act as an electron−hole recombination center. The sample $Bi_2Mo_{0.25}W_{0.75}O_6$ shows the highest activity in the Mo-substituted Bi_2WO_6 samples; a higher content of Mo did not further increase the activity, despite improved photon absorption. This is attributed to the decreased electron mobility and surface area, as discussed above. The incorporation of Mo, resulting in a relatively narrow conduction band with smaller curvature, was not effective for the movement of photogenerated electron−hole pairs, as shown in the electronic structure calculation. The recent work from Yu's group[21] also showed that $Bi_2Mo_{0.25}W_{0.75}O_6$ exhibited the highest photocatalytic activity, even higher than that of Bi_2WO_6, which might be attributed to the different filter ($\lambda > 400$ nm), metal source (W and Mo metal powders), and dye (methylene blue) employed in their work.

The photodegradation of RhB under visible light ($\lambda >$ 450 nm) is further studied to study the effect of Mo replacement; the results are shown in Figure 11. It is observed that $Bi_2Mo_{0.25}W_{0.75}O_6$ shows much higher photocatalytic activity as compared with Bi_2WO_6. The other two samples, $Bi_2Mo_{0.5}W_{0.5}O_6$ and Bi_2MoO_6, also show higher activity than Bi_2WO_6, but lower than $Bi_2Mo_{0.25}W_{0.75}O_6$. The higher performance of Mo-substituted samples under visible light $\lambda > 450$ nm could be attributed to their lower band gap compared with Bi_2WO_6, as shown in diffuse reflectance spectra in Figure 6. It is indicated that the optical absorption property of Bi_2WO_6 could be significantly enhanced by Mo substitution, which is very important from the viewpoint of utilizing solar energy.

CONCLUSIONS

$Bi_2Mo_xW_{1-x}O_6$ photocatalysts were synthesized via a hydrothermal method. The substitution of Mo in Bi_2WO_6 would reduce the conduction band level of Bi_2WO_6 and the curvature of the conduction band. Bi_2WO_6 and $Bi_2Mo_{0.25}W_{0.75}O_6$ showed relatively higher photocatalytic activity than other samples under visible light $\lambda > 420$ nm. $Bi_2Mo_{0.25}W_{0.75}O_6$ shows much higher activity than Bi_2WO_6 under visible light $\lambda > 450$ nm. Mo substitution could effectively reduce the band gap of Bi_2WO_6 and increase the efficiency of utilization of visible light.

ASSOCIATED CONTENT

Supporting Information. PDOS for Bi, Mo, W, and O atoms of Bi_2WO_6 and Bi_2MoO_6. This information is available free of charge via the Internet at http://pubs.acs.org.

AUTHOR INFORMATION

Corresponding Author

*E-mail: zhuyf@tsinghua.edu.cn.

ACKNOWLEDGMENT

This work was supported in part by hte Chinese National Science Foundation (20925725 and 50972070) and the National Basic Research Program of China (2007CB613303). L.Z. acknowledges the Alexander von Humboldt (AvH) Foundation for granting him a research fellowship.

REFERENCES

(1) Fox, M. A.; Dulay, M. T. *Chem. Rev.* **1993**, *93*, 341–357.
(2) Legrini, O.; Oliveros, E.; Braun, A. M. *Chem. Rev.* **1993**, *93*, 671–698.
(3) Fujishima, A.; Honda, K. *Nature* **1972**, *238*, 37–38.
(4) Asahi, R.; Morikawa, T.; Ohwaki, T.; Aoki, K.; Taga, Y. *Science* **2001**, *293*, 269–271.
(5) Khan, S. U. M.; Al-Shahry, M.; Ingler, W. B. *Science* **2002**, *297*, 2243–2245.
(6) Kraeutler, B.; Bard, A. J. *J. Am. Chem. Soc.* **1978**, *100*, 4317–4318.
(7) Sakthivel, S.; Kisch, H. *Angew. Chem., Int. Ed.* **2003**, *42*, 4908–4910.
(8) Kudo, A.; Hijii, S. *Chem. Lett.* **1999**, *10*, 1103–1104.
(9) Tang, J. W.; Zou, Z. G.; Ye, J. H. *Catal. Lett.* **2004**, *92*, 53–56.
(10) Zhang, C.; Zhu, Y. F. *Chem. Mater.* **2005**, *17*, 3537–3545.
(11) Fu, H. B.; Pan, C. S.; Yao, W. Q.; Zhu, Y. F. *J. Phys. Chem. B* **2005**, *109*, 22432–22439.

(12) Zhang, S. C.; Zhang, C.; Man, Y.; Zhu, Y. F. *J. Solid State Chem.* **2006**, *179*, 62–69.
(13) Beale, A. M.; Sankar, G. *Chem. Mater.* **2003**, *15*, 146–153.
(14) Buttrey, D. J.; Vogt, T.; White, B. D. *J. Solid State Chem.* **2000**, *155*, 206–215.
(15) Shimodaira, Y.; Kato, H.; Kobayashi, H.; Kudo, A. *J. Phys. Chem. B* **2006**, *110*, 17790–17797.
(16) Zou, Z.; Ye, J.; Sayama, K.; Arakawa, H. *Chem. Phys. Lett.* **2001**, *343*, 303–308.
(17) Zou, Z.; Ye, J.; Arakawa, H. *Solid State Commun.* **2002**, *119*, 471–475.
(18) Yoshino, M.; Kakihana, M.; Cho, W. S.; Kato, H.; Kudo, A. *Chem. Mater.* **2002**, *14*, 3369–3376.
(19) Zou, Z.; Ye, J.; Arakawa, H. *Chem. Mater.* **2001**, *13*, 1765–1769.
(20) Castro, A.; Bégué, P.; Jiménez, B.; Ricote, J.; Jiménez, R.; Galy *Chem. Mater.* **2003**, *15*, 3395–3401.
(21) Zhou, L.; Yu, M.; Yang, J.; Wang, Y.; Yu, C. *J. Phys. Chem. C* **2010**, *114*, 18812–18818.
(22) David, R. L. *CRC Handbook of Chemistry and Physics*; CRC Press: Boca Raton, FL, 2004−2005.
(23) Hardcastle, F. D.; Wachs, I. E. *J. Raman Spectrosc.* **1995**, *26*, 397–405.
(24) Crane, M.; Forst, R.; Williams, P.; Kloprogge, T. *J. Raman Spectrosc.* **2002**, *33*, 62–66.
(25) Hardcastle, F. D.; Wachs, I. E. *J. Phys. Chem.* **1991**, *95*, 10763–10772.
(26) Gregg, S. J.; Sing, K. S. W. *Adsorption, Surface Area and Porosity*, Academic Press: London, 1982.
(27) Kudo, A.; Tsuji, I.; Kato, H. *Chem. Commun.* **2002**, *73*, 1958–1959.
(28) Zhang, L. W.; Fu, H. B.; Zhang, C.; Zhu, Y. F. *J. Phys. Chem. C* **2008**, *112*, 3126–3133.
(29) Kohn, W.; Sham, L. J. *Phys. Rev. A* **1965**, *140*, 1133–1138.
(30) Perdew, J. P.; Wang, Y. *Phys. Rev. B* **1992**, *45*, 13244–13249.
(31) Payne, M. C.; Teter, M. P.; Allan, D. C.; Arias, T. A.; Joannopoulos, J. D. *Rev. Mod. Phys.* **1992**, *64*, 1045–1097.
(32) The CASTEP program is developed and distributed by Molecular Simulations Inc., San Diego, CA.
(33) Matsushima, S.; Nakamura, H.; Arai, M.; Xu, C. *Chem. Lett.* **2002**, *10*, 700–701.
(34) Xu, J.; Greenblatt, M. *J. Solid State Chem.* **1996**, *121*, 273–277.
(35) Xu, J.; Ramanujachary, K. V.; Hohn, P.; Greenblatt, M. *J. Solid State Chem.* **1996**, *125*, 192–199.